A robust direct-propane solid oxide fuel cell with hierarchically oriented full ceramic anode consisting with *in-situ* exsolved metallic nano-catalysts

Xi Chen[a,c], Jietao Wang[a], Na Yu[a,c], Yao Wang[a,*], Dong Zhang[a], Meng Ni[c], Fanglin Chen[d], Tong Liu[a,b,*], Mingyue Ding[a,*]

[a] Key Laboratory of Hydraulic Machinery Transients (Wuhan University), Ministry of Education, School of Power and Mechanical Engineering, Wuhan University, Wuhan, Hubei 430072, China.

[b] Key Laboratory of Green Chemical Process of Ministry of Education, Key Laboratory of Novel Reactor and Green Chemical Technology of Hubei Province, School of Chemical Engineering and Pharmacy, Wuhan Institute of Technology, Wuhan 430205, P. R. China

[c] Department of Building and Real Estate, Research Institute for Sustainable Urban Development (RISUD) and Research Institute for Smart Energy (RISE), The Hong Kong Polytechnic University, Hung Hom, Kowloon, Hong Kong, China

[d] Department of Mechanical Engineering, University of South Carolina, Columbia, South Carolina 29208, United States

* Corresponding Authors: pmewy@whu.edu.cn (Y. W.), liu_tong@wit.edu.cn (T. L.), & dingmy@whu.edu.cn (M. D.)

Abstract

Perovskite oxide $Sr_2Fe_{1.3}Mo_{0.5}Ni_{0.2}O_{6-\sigma}$ (SFMNi) impregnated on the scaffold of hierarchically oriented yttria-stabilized zirconia (YSZ) with open, straight pores (SFMNi@YSZ), that could be transformed into *in-situ* exsolved Ni-Fe alloy nanoparticles structured SFMNi@YSZ (NiFe@SFMNi@YSZ) electrode, have been prepared and utilized for robust direct propane-fueled solid oxide fuel cell (SOFC). The hierarchically oriented open, straight pores can not only significantly facilitate the introduction of uniformly distributed SFMNi nano-catalyst network via the ion-impregnation method, but also greatly enhance gas diffusion process in the porous electrode, thus greatly minimizing even eliminating the concentration resistance. The impregnated SFMNi nano-catalysts, especially the *in-situ* exsolved Ni-Fe alloy nano-catalysts, could effectively activate the fuel gas oxidation reaction in the anode, thereby drastically decreasing the activation resistance and enhancing the cell performance. The full ceramic electrode can efficiently avoid electrode aggregation and carbon coking, leading to excellent stability towards propane oxidation. Our findings indicate that NiFe@SFMNi@YSZ full ceramic electrode with hierarchically oriented open, straight pores offers a great promise for direct hydrocarbon SOFC.

Keywords: Direct-propane solid oxide fuel cells; Phase inversion tape casting; Full ceramic electrode; *In-situ* exsolution; Infiltration

1. Introduction

To reduce the dependence of modern society on fossil fuels and meet the "3E" criteria (Ecology, Economy & Efficiency), renewable energy utilization and power storage technologies are increasingly important[1-3]. A sustainable energy conversion device based on solid oxide fuel cell (SOFC) has extremely practical value and prospects since it has many remarkable advantages, such as clean operation, efficient conversion from chemicals to electrical energy without limitation of the traditional Carnot cycle, wide fuel flexibility and compactness[4-8].

Some straits still limit the application of hydrogen-fueled SOFCs, such as high cost and hard to store [9, 10]. Given the unique property of high fuel flexibility, SOFCs operating with hydrocarbon fuel is more attractive because of the low price, accessible storage, and higher volumetric energy density of hydrocarbon[11-16]. In addition, with the advantages of high catalytic activity toward fuel oxidation and high operating temperature (⩾600 ºC), SOFCs can directly utilize hydrocarbons without external reformers and fuel processing units, which dramatically simplifies the system and reduces operating costs[17-21].

However, larger hydrocarbon fuel molecules have a slower diffusion rate in the electrode support layer [22, 23]. Taking propane as an example, the diffusion coefficient of propane (0.81 cm^2/s) is much smaller than that of hydrogen (5.35 cm^2/s) under the same humidified atmosphere at 750 °C [24], so it is difficult for hydrocarbon fuels to reach the active reaction sites, causing the sluggish reaction process and thus limiting the electrochemical performance [12, 25-27]. Moreover, the classic sponge-like electrode prepared by traditional dry pressing has low porosity and high tortuosity, which is not conducive to the diffusion of fuel gas[5, 28-31]. Thus, it's necessary to enhance the mass transport process of hydrocarbon fuels by optimizing the microstructure of the

electrode.

In addition, the direct use of hydrocarbon fuels will lead to carbon deposition on the traditional Ni-based anode, which will deactivate the catalyst and cause significant degradation in performance[12, 32-36]. Many works have shown that impregnating perovskite-type oxides nano-catalysts in the electrode supporting layer is an effective way to improve the carbon tolerance of electrodes[26, 37-43]. However, the infiltration process is not suitable for the traditional electrodes since they have many tortuous micropores, which leads to poor dispersion of impregnated nanoparticles (NPs)[26, 44]. Although Chen et al. prepared an open-pore Ni-based anode supporting layer by freeze-drying tape casting method, it's fragile and weak, especially after treatment in a reducing atmosphere since intensive pores will be formed[26, 45]. Therefore, it's urgent to improve the electrode microstructure and select a suitable impregnated skeleton to simplify the infiltration process, improve the uniformity of the infiltrated phase, and thus enhance the overall mechanical strength of the cell.

Meanwhile, perovskite-based oxides such as $Sr_2Fe_{1.5}Ni_{0.2}Mo_{0.5}O_{6-\delta}$ (SFMNi), Co doped $Pr_{0.5}Ba_{0.5}MnO_{x,}$ and La and Ni co-doped $SrTiO_3$, modified by *in-situ* exsolved metallic nanoparticles catalysts, display improved catalytic activity, long-term stability, redox stability, and particularly resistance to carbon coking[12, 46-51]. In a reducing atmosphere or applying electrical potentials, the parent perovskite material will *in-situ* generate B-site metal nanoparticles, which are uniformly and firmly pinned into the parent perovskite-based oxide surface, forming a unique composite electrode with the strong interactions between metal nano-catalysts and parent matrix lattice, which is beneficial for Electron-ion fast transport at metal-oxide interfaces. Most importantly, the strong adhesion interface between *in-situ* exsolved nanoparticles and parent oxide, exhibits superior carbon

81 tolerance, most notably inhibiting catalyst particle uplift and subsequent carbon fiber formation[46,
82 52-54]. These highlight merits made this novel strategy very suitable and essential for direct
83 hydrocarbon-fueled SOFCs.

84 Herein, a hierarchically oriented yttria-stabilized zirconia (YSZ) support framework with open,
85 straight pores was prepared by a novel phase inversion co-tape casting method (PITC)[22, 55-59].
86 SFMNi nanoparticles with high catalytic activity and stability[60-62], which could be further
87 transformed into NiFe alloy nanoparticles structured SFMNi (NiFe@SFMNi) nano-catalysts in a
88 reducing atmosphere, were impregnated into the inner surface of the open, straight pores, thereby
89 effectively improving the dispersion of the nano-particles catalyst and significantly enhancing the
90 electrochemical performance of the symmetrical cell. Under a reducing atmosphere, the infiltrated
91 SFMNi parent perovskite can be *in-situ* transformed into NiFe@SFMNi nano-catalysts, thus
92 forming NiFe@SFMNi infiltrated hierarchically oriented YSZ electrode with open, straight pores
93 (NiFe@SFMNi@YSZ electrode). The anchoring connection of the nanoparticles and the matrix
94 perovskite enable the catalysts to have excellent anti-coking performance, thereby achieving high
95 catalytic activity and stability in the oxidation of hydrocarbon fuels[12, 46]. This novel nanoparticle-
96 modified porous electrode combines multiple advantages: (1) The electrode support layer with
97 vertical gradient open pores is prepared in one step by the phase inversion tape-casting method,
98 which effectively accelerates the gas diffusion process of hydrocarbon fuels; (2) The hierarchically
99 oriented YSZ skeleton with open, straight pores significantly simplify the infiltration process, and
100 improves the dispersion process of the infiltrated nanoparticles, and thus enhancing the mechanical
101 strength and electrochemical performance of the cell; (3) the infiltrated SFMNi phase, especially
102 the *in-situ* formed and strongly anchored NiFe alloy nanocatalysts, could effectively accelerate the

oxidation reaction of hydrocarbon fuel and enhance the anti-carbon coking performance of the cell.

2. Experimental section

2.1 Preparation of the single cells and symmetrical cells

The process for preparing the hierarchically oriented porous electrode layer with straight pores via the novel PITC method is schematically shown in Figure 1. Initially, two typical slurries, yttria-stabilized zirconia (YSZ) slurry, and graphite slurry were prepared by planetary ball-milling the raw materials (Step 1 in Figure 1), which are listed in Table S1. The homogenous slurries are ball-milled for 24 hours, and then co-cast on a polyether imide (PEI) mylar film to form a precursor electrode substrate after putting both slurries in a vacuum pump for 30min to eliminate bubbles (Step 2 in Figure 1), which is then transferred to a deionized water bath to complete the phase inversion process (Step 3 in Figure 1). Finally, the dried green electrode substrate is cut into disks with diameters of 6 and 13 mm by using a laser (Step 4 in Figure 1).

The schematic diagram of the preparation procedure of the symmetrical solid oxide fuel cell (SSOFC), made of a hierarchically oriented electrode with straight pores, is also summarized in Figure 1. Two cut electrode substrates with diameters of 6 and 13 mm are both drop-coated with the prepared electrolyte slurry to form two YSZ electrode support/YSZ electrolyte bilayer precursors (Step 5 in Figure 1), which are then co-pressed to achieve triple-layer skeleton precursor with a structure of YSZ electrode support framework/YSZ electrolyte/YSZ electrode support framework by using a warm isostatic press method (Step 6 in Figure 1) under a constant force of 20 N with a dwell time of 10 min at 80 °C (Techson P64, China). Then, the triple-layer skeleton precursor is sintered at 1400 °C for 5 hours to obtain a triple-layer skeleton (Step 7 in Figure 1), which is finally infiltrated with $Sr_2Fe_{1.5}Mo_{0.5}O_{6-\delta}$ (SFM) and SFMNi precursor solution and calcined at 850 °C for

5 hours to form the expected SFM@YSZ/YSZ/SFM@YSZ single cell and SFMNi@YSZ/YSZ/SFMNi@YSZ single cell, respectively (Step 8 in Figure 1). Note that Table S1 summarizes the specific compositions of the YSZ electrolyte slurry, while Table S2 gives the detailed composition of the SFM and SFMNi precursor infiltration solutions.

The preparation process of the symmetrical cells, which were used for the electrode reaction process study eliminating the influence of the other electrode, is the same as that of the single cells, and the only difference is that two 13-mm green electrode support precursors are used for the preparation via the similar preparation procedure. In this work, the effective area of the single cells and symmetrical cells is measured to be 0.25 and 0.82 cm^2, respectively.

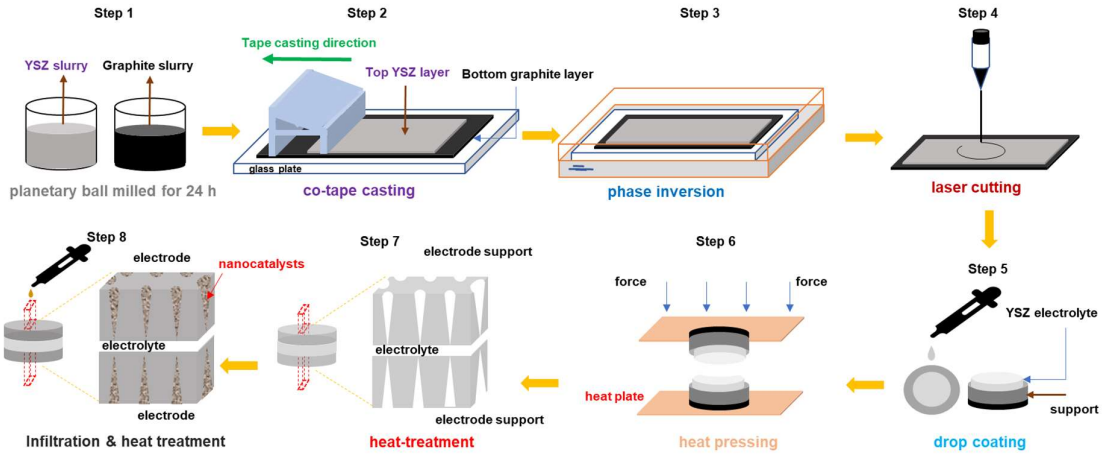

Figure 1 Schematic diagram of the preparation procedure of the symmetrical single cells used for direct propane solid oxide fuel cells.

2.2 Characterization

The X-ray diffraction (XRD, Xpert Pro) is used to record the crystal structure of the SFM@YSZ and SFMNi@YSZ electrodes to determine phase transition before and after reduction, while the X-ray photoelectron spectroscopy (XPS, ESCALAB250Xi) is applied to collect characterize the evolution of the valence states. In addition, high-resolution transmission electron microscope

(HRTEM, JEM-2010F) as well as scanning electron microscope (SEM, Tescan MIRA 3) is utilized to collect the morphology of the cells and the electrodes. Moreover, the X-ray energy spectrometer (EDS, Aztec Energy, Oxford instruments) is adopted to collect the element distributions.

2.3 Electrochemical test

The prepared symmetric cell is placed in a tube furnace which exposed to wet hydrogen while the gas flow rate is 30ml/min which controlled by a mass flow meter (APEX, Alicat Scientific). The electrochemical impedance spectroscopy (EIS) was recorded by electrochemical workstation (Zennium E, Zahner, Germany) under open circuit voltage (OCV) in the frequency range of 10^6–10^{-2} Hz with a voltage amplitude of 30 mV. Electrochemical performance measurements of single cells were performed on a home-made shaft using the above mentioned electrochemical workstation. After sealing the single cell to the alumina tube by conductive glue and ceramic adhesive, the anode and cathode were exposed to humidified flowing fuel gas and ambient air, respectively. The gas flow rate of the wet hydrogen is 30 ml/min, while that of wet propane is 20ml/min. The EIS was recorded under OCV in the frequency range of 10^6–10^{-2} Hz with a voltage amplitude of 30 mV. The current density-voltage-power density (*i*-V-p) curves were obtained by linear scanning with the voltage range from OCV to 0 V under the hydrogen fuel, while that was from OCV to 0.2 V under the propane fuel, and the scanning rate was 30 mV/s. Note that more detailed descriptions have been included in the supporting information.

3. Results and Discussion

Figure 2a and 2b show the top view and bottom view photographs for the YSZ/graphite bilayer precursor electrode substrate prepared by the PITC method, and a homogeneous white YSZ/black

165 graphite bilayer electrode substrate with a size larger than 150mm×250mm is obtained, suggesting
166 that PITC method is an effective preparation method to prepare commercial electrode substrate.
167 Figure 2c presents the cross-sectional SEM image of the prepared YSZ/graphite bilayer precursor
168 electrode substrate, which is constitutive of a thick layer with hierarchically oriented straight pores
169 and a thin layer with sponge-like pores. After sintering at 1400 ºC for 5 hours, the thin sponge-like
170 layer has been effectively removed (Figure 2d). In addition, the bottom view SEM image shown in
171 Figure 2e confirms the elimination of the sponge-like layer and the formation of open pores. These
172 results indicate that the sponge-like layer is derived from the graphite slurry and consisted of PESf
173 and graphite, while the thick layer with hierarchically oriented straight pores is strongly associated
174 with the YSZ slurry and could maintain its structure after heat treatment. On the other hand, as
175 shown in the top view SEM image (Figure 2f) that a very thin skin layer with sponge-like pores is
176 formed at the YSZ slurry/H_2O bath interface. These results demonstrate the formation of unique
177 hierarchically oriented electrode support with open, straight pores. It should be pointed out that the
178 thin skin layer is suitable for the deposition of thin electrolyte film and capable of the functional
179 layer for oxygen reduction reaction (ORR) or hydrogen oxidation reaction (HOR), while the
180 hierarchically oriented electrode support with open, straight pores could provide fast gas transports
181 channels, implying that this unique electrode structure is an ideal one for SOFC.

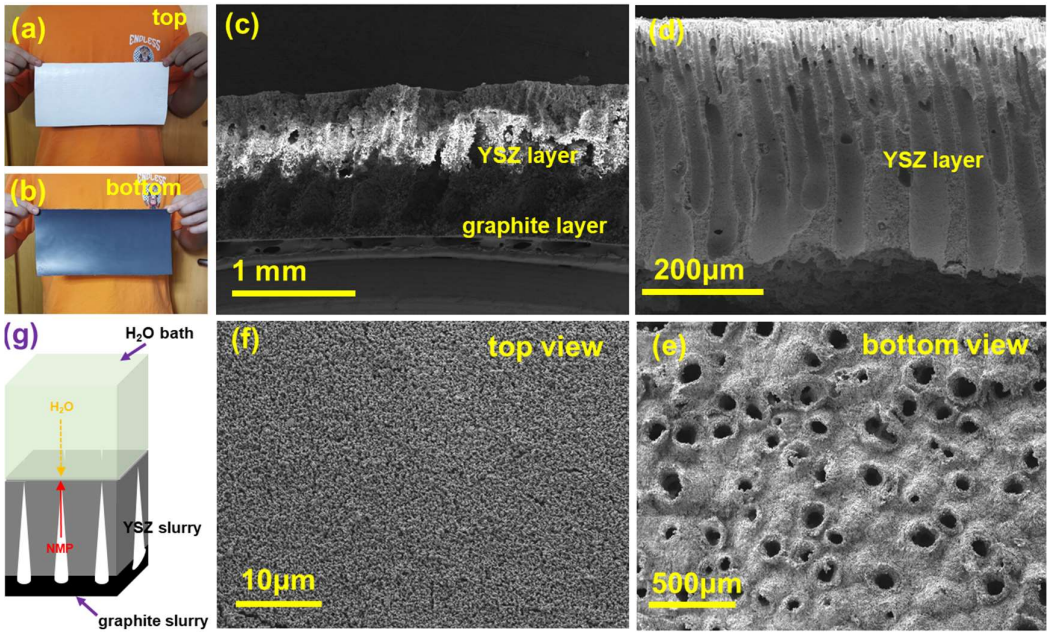

Figure 2 (a) Top view and (b) bottom view photographs of the YSZ/graphite bilayer precursor electrode substrate prepared by the PITC method, cross-sectional SEM images of (c) precursor electrode substrate and (d) the YSZ electrode skeleton sintered at 1400 ºC for 5 hours, (e) bottom view and (f) top view SEM images of the as-sintered YSZ electrode skeleton, and (g) the schematic diagram of the formation mechanism of the straight pores during the phase inversion process.

At the same time, a schematic diagram is illustrated in Figure 2g to better explain the formation mechanism of this unique structure according to the previously reported literature. On one hand, an immediate and ultrafast NMP/H_2O exchange will occur as the co-tape cast YSZ slurry/graphite slurry containing NMP solvent is immersed into the non-solvent H_2O bath, resulting in thick finger-like straight pores in the precursor electrode substrate. On the other hand, a thin sponge-like layer is formed at the interface of graphite slurry/PEI mylar film, which is possibly associated with the slow precipitation of PESf phase in the phase inversion slurry due to the insufficient non-solvent H_2O for NMP/H2O exchange rate. Therefore, a bilayer structure, consisting of a thick hierarchically oriented straight pores layer and a thin sponge-like layer, is achieved during the PITC process.

To confirm the superiority of the hierarchically oriented straight pores structure prepared by the PITC method, two electrodes supports with sponge-like pores, were prepared by using the drying pressing method and sacrificing the 20 wt.% graphite or 20 wt.% polymethyl methacrylate (PMMA) as the pore former, has been also studied. We found that a low tortuosity factor close to 1 is obtained for the hierarchically oriented straight pores electrode supported prepared by the PITC method when compares with the other two although they have similar porosity of approximately 55% (Figure 3a-c). Additionally, it is interestingly observed from the contact angle (CA) images (Figure 3d-f) that after dropping the SFMNi infiltration solution on the electrode surface, the water drop is completely absorbed by the hierarchically oriented straight pores electrode support, and the CA value is decreased from 16.3 to 6.0 ^{o} after 2 seconds, and further to 0 ^{o} at the 3rd second (Figure 3g). However, for the other two electrode supports, the CA value is greatly 38.0 and 30.6 to 29.0 and 16.8 ^{o} even after maintaining for 6 seconds (Figure 3g), respectively, indicating the water drop cannot be immediately absorbed by the electrode supports. The lowest initial CA value and fastest water absorption rate reveal the best hydrophilicity towards infiltration solution so that the nano-catalysts can be infiltrated more rapidly and distributed more uniformly in the entire electrode skeleton, suggesting that the hierarchically oriented straight pores benefit the introduction of SFMNi and SFM nano-catalysts in the electrode support via the conventional solution infiltration technique. This finding was more intuitively demonstrated by the dynamic process of solution infiltration that was depicted in the supporting information video. Moreover, nitrogen (N_2) permeation results in Figure 3h demonstrate that the N_2 permeability for the hierarchically oriented straight pores electrode support is measured to be 78.20±1.12 ×10^{5} L h^{-1} m^{-2} bar^{-1}, which is significantly higher than 5.89±0.22 ×10^{5} and 2.24±0.12 ×10^{5} L h^{-1} m^{-2} bar^{-1} for the sponge-like electrode support

framework prepared by the addition of graphite and PMMA as the pore former, respectively, meaning the hierarchically oriented straight pores can serve as the active channels for fast gas transport in the electrode. The improved nano-catalysts' introduction simplicity, excellent gas permeability, and significantly low tortuosity make the hierarchically oriented electrode support with open, straight pores prepared by the PITC method capable of a more promising electrode support candidate than the others.

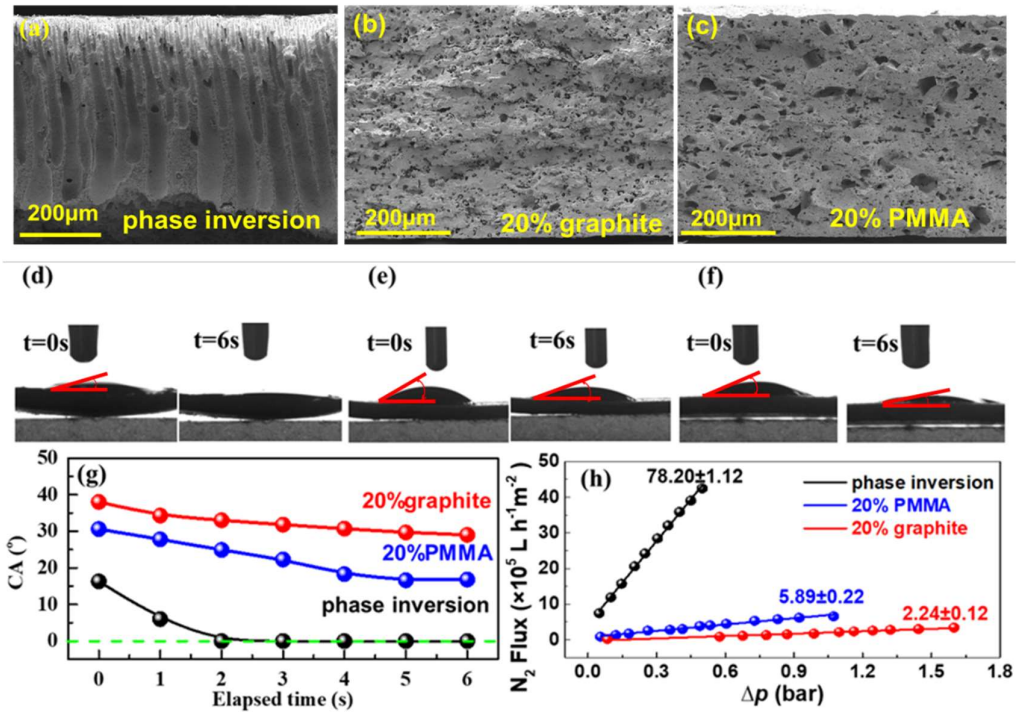

Figure 3 (a-c) Cross-sectional SEM images, (d-f) contact angles images, (g) contact angle evolution after impregnation of infiltration solution, and (h) N_2 permeability for the anode substances prepared by the phase inversion tape casting method, and the addition of 20% graphite and 20% PMMA as pore former, respectively.

Figure 4a presents the cross-sectional SEM image of the SSOFC with SFMNi nano-catalysts decorated hierarchically oriented straight pores electrode, and a well-constructed SSOFC with three typical layers, marked as hierarchically oriented open straight pores electrodes (cathode and anode),

thin electrolyte film, has been successfully fabricated by the combined warm isostatic pressing, ion impregnation, and heat-treatment process. The unique structure, hierarchically oriented straight pores with significantly low tortuosity, has been effectively retained during the SSOFC assembly process (Figure 4b). At the same time, the surface of the straight macro-pores before and after the addition of SFMNi nano-catalyst has been further recorded by the enlarged SEM images shown in Figure 4c-d. It is clearly shown that the smooth surface of the bare YSZ skeleton has been effectively covered by a homogeneous layer with nano-sized powders.

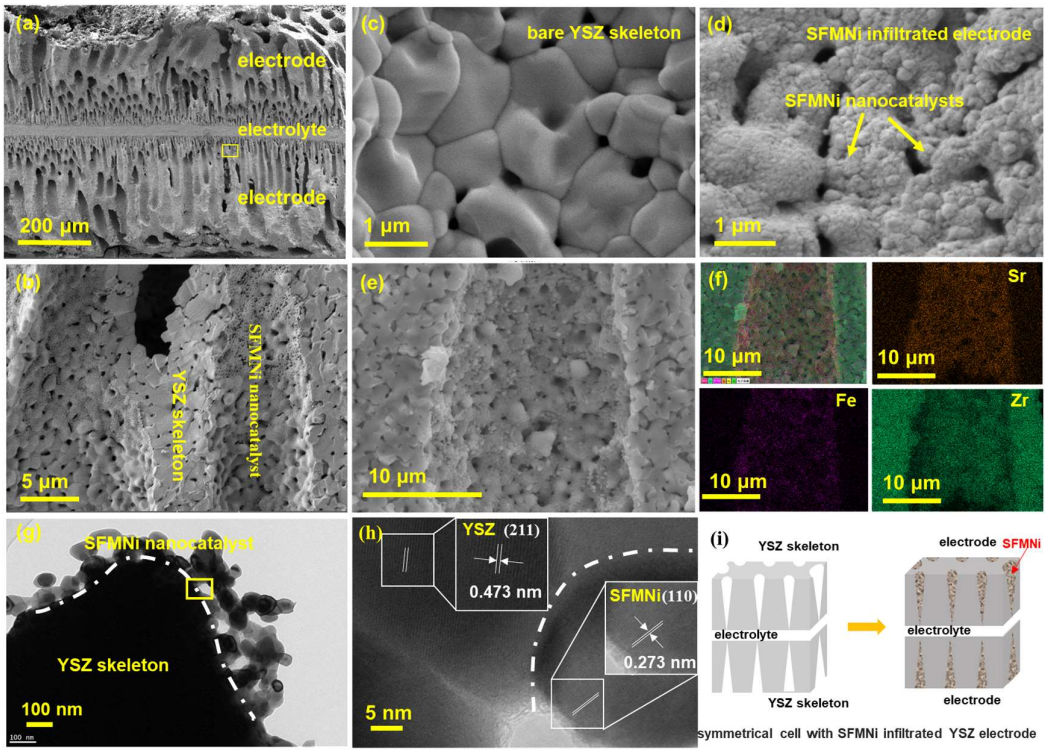

Figure 4 (a) Cross-sectional SEM image of symmetrical cell with SFMNi nano-catalysts infiltrated YSZ electrodes (SFMNi@YSZ), (b) enlarged cross-sectional SEM image of marked area shown in Figure 4a, SEM images of the surface of straight pores (c) before and (d) after SFMNi infiltration, (e) SEM and (f) EDS images of the cross-section of SFMNi@YSZ electrode, (g-h) HRTEM images of the cracked SFMNi@YSZ electrode, and (i) the schematic diagram of the preparation of the

symmetrical cell with SFMNi@YSZ electrodes.

Moreover, the SEM images as well as its elemental mappings of the SFMNi@YSZ electrode including the chemical elements Sr $K_{\alpha 1}$, Fe $K_{\alpha 1}$, and Zr $L_{\alpha 1}$, representing the infiltrated SFMNi phase and the YSZ skeleton phase, are collected (Figure 4e-f). According to the result of the distribution of the characteristic elements, we further demonstrate that the impregnated nano-sized SFMNi particles are well-adhered to the inside surface of the open, straight pores, while the wall of the YSZ skeleton maintains its intrinsic morphology without any adverse effect during the infiltration process. In a word, the bare YSZ skeleton with a smooth inner surface has a hierarchically oriented open straight-pore microstructure, which can be effectively maintained after infiltrating the SFMNi nano-particles. In addition, the infiltrated SFMNi nano-particles are uniformly distributed on the inner surface and tightly combined to effectively form the interconnected conductive network, so that it can effectively increase the specific surface area and electrical conductivity of the electrode simultaneously, thereby significantly enhancing the electrochemical performance of the single cells. This can also be verified by the TEM results shown in Figure 4g-h. As shown in Figure 4g that the impregnated SFMNi nanoparticles are tightly packed on the YSZ skeleton, and the SFMNi nanoparticles are well-connected to each other into a conductive porous network. Additionally, two distinct phases presented by the different d-spacings of 4.73 and 2.73 Å, which are calculated from the enlarged HRTEM image Figure 4h), can be observed at the interface of these two phases, and correspond to the (211) plane of YSZ skeleton and the (110) plane of SFMNi phase, respectively. These results all indicate that a conductive SFMNi network is well-connected to the YSZ skeleton to successfully form SFMNi@YSZ nanostructured hierarchically oriented electrode with open, straight pores by infiltrating the infiltration solution into the YSZ skeleton (Figure 4i).

To further investigate the formation of the desired nanostructured electrode and confirm the chemical compatibility of the infiltrated phase and YSZ skeleton, the phase compositions of the YSZ powders, SFM powders, SFMNi powders, SFM@YSZ electrode, and SFMNi@YSZ electrode are evaluated by the XRD and summarized in Figure 5b. As expected, the single-phase perovskite oxide SFM and SFMNi powders can be obtained by pre-heating their corresponding infiltration solutions under the same condition as the infiltration process. Additionally, all detected characteristic peaks for the as-prepared infiltrated electrodes (SFM@YSZ and SFMNi@YSZ electrodes) correspond to the phases of perovskite-type SFM/SFMNi and fluorite-type YSZ without any impurity phase after heat-treatment at 900°C for 5h in air, indicating the formation of the expected SFM/SFMNi@YSZ electrodes via the infiltration technique and the outstanding chemical compatibility between SFM/SFMNi and YSZ after heat-treatments.

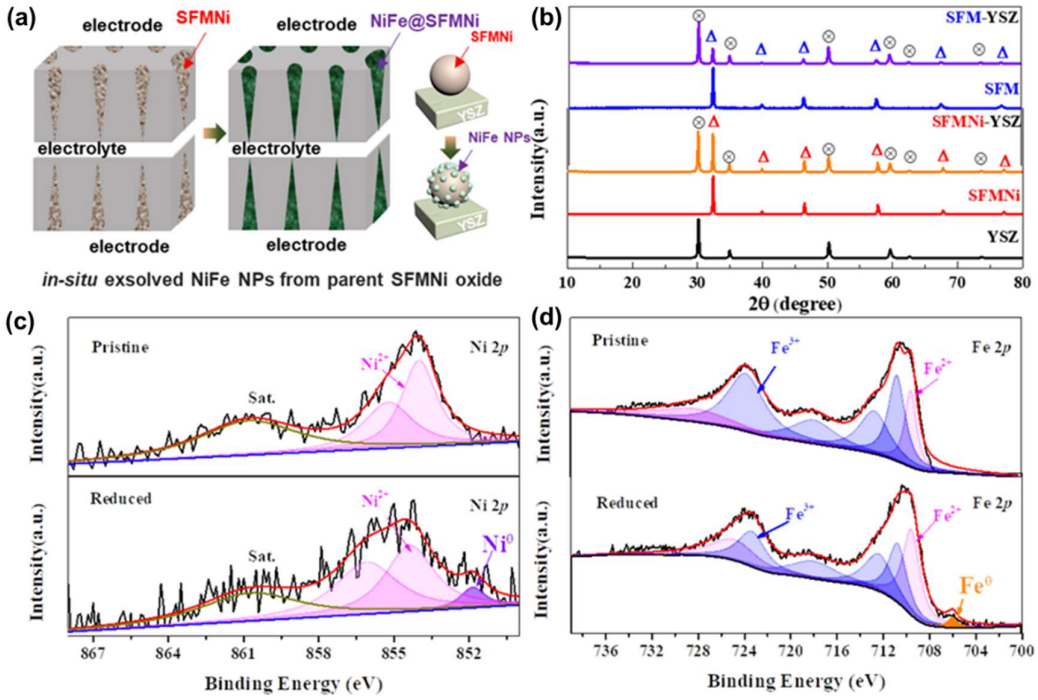

Figure 5 (a)The schematic diagram of the in-situ exsolved NiFe NPs from the parent SFMNi oxide; (b) XRD patterns of YSZ powders, SFM powders, SFMNi powders, SFM infiltrated YSZ electrode

282 and SFMNi infiltrated YSZ electrode, and (c-d) XPS spectra of the core level regions of the cracks

283 of pristine and reduced SFNMi infiltrated YSZ electrode, (c) Ni 2p, and (d) Fe 2p.

284 At the same time, to further verify the *in-situ* exsolution of NiFe nanoparticles from the infiltrated

285 SFMNi phase, the elemental compositions and valence states of SFMNi@YSZ electrode before and

286 after reduction in 3%H_2O humidified H_2, schematically shown in Figure 5, are studied by the XPS

287 measurements (Figure S1). All the elements for the SFMNi@YSZ electrode, including Sr, Fe, Mo,

288 Ni, O, Y, and Zr, can be observed in the XPS spectra, identifying the co-presence of SFMNi phase

289 and YSZ phase, which is consistent with the results shown in Figure 4f-h and Figure 5b. In addition,

290 the collected core level regions of Ni 2p and Fe 2p shown in Figure 5c-d are fitted to confirm the

291 formation of NiFe nanoparticles from the parent infiltrated SFMNi phase via the *in-situ* exsolution

292 technique. For the fresh SFMNi@YSZ electrode sample, only the characteristic peaks for Ni^{2+},

293 centered at the binding energy of ~855 and ~861.4 eV, have been determined (Figure 5c), while two

294 obvious valence states of Fe^{2+} and Fe^{3+} are observed for Fe $2p_{3/2}$ core-level XPS spectra and

295 confirmed by the fitted peaks located at the binding energies of 709.8 and 710.8/711.6/719.2 eV,

296 respectively (Figure 5d). As anticipated, after reduction treatment, the characteristic peaks for Ni^{2+},

297 Fe^{2+}, and Fe^{3+} can be also maintained, on contrast, additional peaks centered at 852.6 and 706.8 eV

298 are simultaneously detected, which are strongly assigned to Ni^0 and Fe^0, respectively, confirming

299 the formation of NiFe alloy phase via the *in-situ* exsolution technique, which also highly agrees

300 with the observation of $FeNi_3$ alloy phase reported by previous literature[60, 63-65]. These results

301 also indicate the successful preparation of *in-situ* exsolved NiFe alloy nanoparticles structured

302 SFMNi@YSZ electrode (NiFe@SFMNi@YSZ).

303 Electrode polarization resistance, R_p, also called area-specific resistance (ASR), is usually used

304 to evaluate the electrochemical performance of the electrode, and the lower R_p value suggests the
305 higher electro-catalytic activity of the electrode. Therefore, the R_p values for the symmetrical cells
306 with bare YSZ electrode skeleton, SFM@YSZ electrode, and SFMNi@YSZ electrode, which have
307 the configuration of YSZ/YSZ/YSZ, SFM@YSZ/YSZ/SFM@YSZ, and
308 SFMNi@YSZ/YSZ/SFMNi@YSZ, respectively, are recorded and calculated by using the EIS
309 results in 3%H_2O humidified H_2 atmosphere. Meanwhile, to avoid the electrolyte effect, the ohmic
310 resistance (R_{ohmic}), which corresponds to the high-frequency intercept of the Nyquist plot with the
311 *x*-axis, has been simplified to zero. It can be observed from Figure S2 that the R_p value for the YSZ
312 electrode skeleton is measured to be 863.12 Ω cm^2, which is 3 orders of magnitude higher than the
313 infiltrated YSZ electrodes shown in Figure 6a. After the infiltration of SFM nano-catalysts, a
314 significantly low R_p value of 0.56 Ω cm^2 is obtained for the SFM@YSZ electrode, indicating the
315 good electrocatalytic activity of the infiltrated SFM nanocatalysts towards hydrogen oxidation
316 reaction (HOR) as well as the good electrical conductivity of the infiltrated phase. Moreover, it is
317 fortunately found that the R_p value is further decreased by nearly 71% compared with the
318 SFM@YSZ electrode from 0.56 to 0.16 Ω cm^2 for SFMNi nanoparticles infiltrated YSZ electrode.
319 The enhancement of the electrode electrochemical performance is greatly associated with the
320 different infiltrated phases. Compared with the SFM phase, the SFMNi phase can be transformed
321 to the NiFe@SFMNi phase, and the *in-situ* exsolved NiFe alloy nanoparticles can strongly
322 accelerate the HOR. At the same time, the R_p value is increased to only 0.28 Ω cm^2 for the
323 SFMNi@YSZ electrode when the operating temperature is lowered to 700°C (Figure S3). Moreover,
324 the outstanding electrochemical performance of SFMNi@YSZ electrode is found to be much higher
325 than others ever reported $SrFeO_3$-based ceramic electrodes as summarized in Table 1, further

326 confirming the superiority of these infiltrated electrodes with *in-situ* exsolved alloy nano-catalysts
327 and hierarchically oriented open, straight pores[66-73].

328 Herein, the distribution of relaxation times (DRT) technique is also performed to further analyze
329 the measured EIS results shown in Figure 6a, and then determine each sub-step and the rate-
330 determining sub-step of the electrode reaction processes, which is because the enclosed area of each
331 peak is equal to each sub-resistance for sub-step of the electrode reaction process. As shown in
332 Figure 6b, three typical DRT peaks are clearly identified in the calculated DRT results and marked
333 as P1-P3 from low to high frequency, and the sub-steps related to the P2 and P3 peaks predominately
334 determine the electrode reaction process due to the larger enclosed area compared with P1 peak.
335 Moreover, according to the results reported in the previous literature[74-77], P2 and P3 peaks in the
336 DRT results, located at the frequency ranges of 10^1-10^3 Hz and above 10^3 Hz, corresponding to the
337 electrode electrochemical reactions, such as charge transfer, surface diffusion, and oxygen ion (O^{2-})
338 bulk diffusion to three phase boundaries (TPBs) processes. That indicated this improvement may be
339 due to the in-situ exsolved nano-catalyst which enlarged electro-active reaction sites where the
340 electrochemical reaction occurs since the typical peaks P2 and P3 are strongly lowered and their
341 corresponding resistances (R_{P2} and R_{P3}) are greatly decreased. Additionally, the stability of the
342 electrochemical performance of SFMNi@YSZ electrode is also studied to verify the possibility for
343 durable SOFC application by recoding the R_p values at varied elapsed times. Figure 6c presents the
344 evolution of the R_p value of the symmetrical cell with SFMNi@YSZ electrodes as a function of the
345 elapsed time when operated at 750 °C and 3%H_2O humidified H_2. During the nearly 110-hour
346 operation, the R_p value varied in the narrow range of 0.26±0.01 Ω cm^2, fully demonstrating the
347 excellent durability of electrochemical reaction and catalytic activity for the SFMNi@YSZ

electrode during operation.

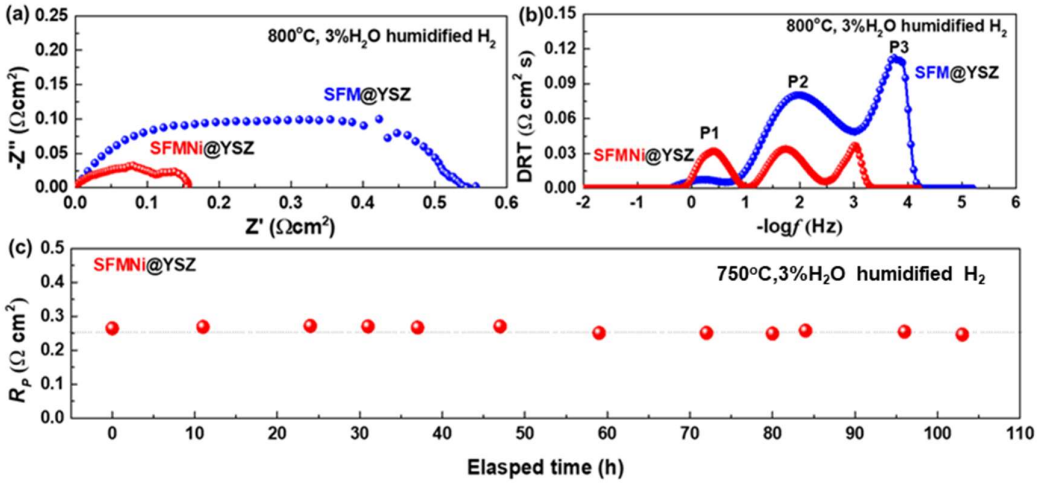

Figure 6 (a) The recorded EIS for the symmetrical cells assembled with SFM@YSZ or SFMNi@YSZ electrodes measured at 800 °C and 3%H_2O humidified H_2, (b) DRT analysis results of the EIS shown in Figure 6a, and (c) the R_p value of the symmetrical cell with SFMNi@YSZ electrodes as a function of the elapsed time when operated at 800 °C and 3%H_2O humidified H_2.

Table 1. Comparison of the R_p values of $SrFeO_3$ based ceramic electrodes determined with symmetrical cells in wet H_2 atmosphere

Electrodes	Temperature(°C)	Rp (Ω cm^2)	Refs
$Sr_2Fe_{1.5}Mo_{0.5}O_{6-\sigma}$	750	0.46	63
$Sr_2Fe_{1.3}Ni_{0.2}Mo_{0.5}O_{6-\sigma}$	750	0.96	64
$La_{0.7}Sr_{0.3}Ti_{0.1}Fe_{0.6}Ni_{0.3}O_{3-\sigma}$	750	0.267	65
$Sr_2Fe_{1.3}Mo_{0.5}Ni_{0.2}O_{6-\sigma}$-YSZ	750	0.20	This work
$SrFe_{0.75}Mo_{0.25}$-8%YSZ	800	0.79	66
$Sr_2Fe_{1.4}Ni_{0.1}Mo_{0.5}O_{6-\sigma}$	800	0.65	64
$Pr_{0.8}Sr_{1.2}(Co,Fe)_{0.8}Nb_{0.2}O_{4+\sigma}$	800	0.44	67

$Sr_2Fe_{1.5}Mo_{0.5}O_{6-\sigma}$	800	0.356	68
$Sr_2Fe_{1.5}Mo_{0.5}O_{6-\sigma}$	800	0.31	69
$Sr_2Fe_{1.5}Mo_{0.5}O_{6-\sigma}$	800	0.27	63
$Sr_2Fe_{1.5}Mo_{0.5}O_{6-\sigma}$-$Sm_{0.2}Ce_{0.8}O_{1.9}$	800	0.25	68
$La_{0.7}Sr_{0.3}Ti_{0.1}Fe_{0.6}Ni_{0.3}O_{3-\sigma}$	800	0.202	65
$Sr_{1.7}Ca_{0.3}Fe_{1.5}Mo_{0.5}O_{6-\sigma}$	800	0.19	69
$Sr_2Fe_{1.5}Mo_{0.5}O_{6-\sigma}$	800	0.23	70
$Sr_{1.85}Ca_{0.15}Fe_{1.5}Mo_{0.5}O_{6-\sigma}$	800	0.12	69
$Sr_2Fe_{1.5}Mo_{0.5}O_{6-\sigma}$-YSZ	800	0.56	This work
$Sr_2Fe_{1.3}Mo_{0.5}Ni_{0.2}O_{6-\sigma}$-YSZ	800	0.16	This work

Taking advantage of the good electrochemical performance and excellent stability of the SFMNi@YSZ electrode with hierarchically oriented open, straight pores, the SSOFC assembled with two SFMNi@YSZ electrodes is fabricated, and its electrochemical performance, including the *i-V-p* curves and EIS results, are collected by exposing the SFMNi@YSZ anode and SFMNi@YSZ cathode to 3%H_2O wet H_2 and ambient air, respectively. It can be seen from the *i-V-p* curves measured at 700°C-800°C shown in Figure 7a, all the obtained open circuit voltage (OCV) values of the single cell are larger than 1.0 V, which are close to the theoretical values calculated by the Nernst equation, indicating that the single cell is well-prepared and well-sealed without obvious gas leakage. Moreover, the peak output power density (P_{max}) of this SSOFC can reach 155 mW cm^{-2} at 800 °C. In addition, in terms of the corresponding EIS results (Figure 7b), the R_{ohmic} values are

determined to be 1.87, 1.49, and 1.36 Ω cm^2 at 700, 750, and 800 °C, respectively, while the corresponding R_p values are calculated to be 1.46, 0.93, and 0.55 Ω cm^2. These results could be explained by the increased oxygen ion conductivity and the enhanced electro-catalytic activities at elevated temperatures. The EIS results shown in Figure 7b are also analyzed and the electrode reaction process is effectively separated with the help of the DRT method to reveal the specific sub-steps of the electrochemical reaction, the final DRT results are shown in Figure 7c. Five characteristic peaks, indexed as P1, P2, Padd1, P3, and Padd2 from low frequency to high frequency, are observed during the measured frequency range (10^{-2}-10^{6} Hz), indicating that the electrode reaction is dominated by at least 5 different sub-steps in the operating temperature range. According to the reports about the typical frequency range of peaks in the literature[78-81], the P1 peak located at the frequency range of 10^{-1}-10^{0}Hz corresponds to the gas diffusion process, while the P2 and Padd1 peaks in the frequency range of 10^{0}-10^{3}Hz are related to the gas conversion process, such as the gas adsorption and desorption sub-steps. Additionally, P3 and Padd2 peaks appear in the frequency above 10^{3} Hz are often associated with electrode electrochemical reaction processes such as charge transfer and surface diffusion. Moreover, these characteristic peaks show different trends as the operating temperature changes. When the working temperature increases, the low-frequency characteristic peak P1 does not change and remains relatively small compared with other peaks, while the intermediate-frequency characteristic peaks P2 and Padd1 as well as the high-frequency characteristic peaks P3 and Padd2 will decrease, among which P2 and P3 peaks have the largest reduction rate. It is further confirmed that the gas diffusion process does not slow down with increasing temperature, which is strongly due to the excellent electrode pore structure. Additionally, the rise of working temperature can effectively accelerate other sub-steps during the electrode

electrochemical reaction.

The stability of the electrochemical performance of the SSOFC is also tested by collecting and separating the typical total resistance at 750 °C. The cell is very stable, and the measured OCV value maintains at 1.04 V during the durability testing (Figure S4a). After nearly 80-hour testing, the R_p value slightly reduces from the initial value of 0.93 to 0.84 Ω cm^2, and finally remains stable. The R_{ohmic} value increases slightly from 1.49 to around 1.60 Ω cm^2 (Figure 7d). The R_p value undergoes a self-activation process probably because the NiFe alloy nano-catalysts can continuously exsolve from the impregnated SFMNi nanoparticles in the reducing surrounding environment, promoting the electrochemical reaction. At the same time, when operated at the constant working voltage of 0.8 V, the current density of the cell is stable at 95 mA cm^{-2}, indicating good stability (Figure S4b). In addition, after working for 69 hours, the p_{max} value of the cell doesn't decrease, but slightly increases (Figure S4c), which is consistent with the slightly decreased R_{total} value shown in Figure 7d. It can be concluded that the *in-situ* exsolved NiFe nano-catalysts, riveting on the surface of the impregnated nanoparticles, are responsible for the self-improvement and the stable state of the cell, indicating the SFMNi@YSZ electrode is a greatly promising stable electrode in the application of SSOFC

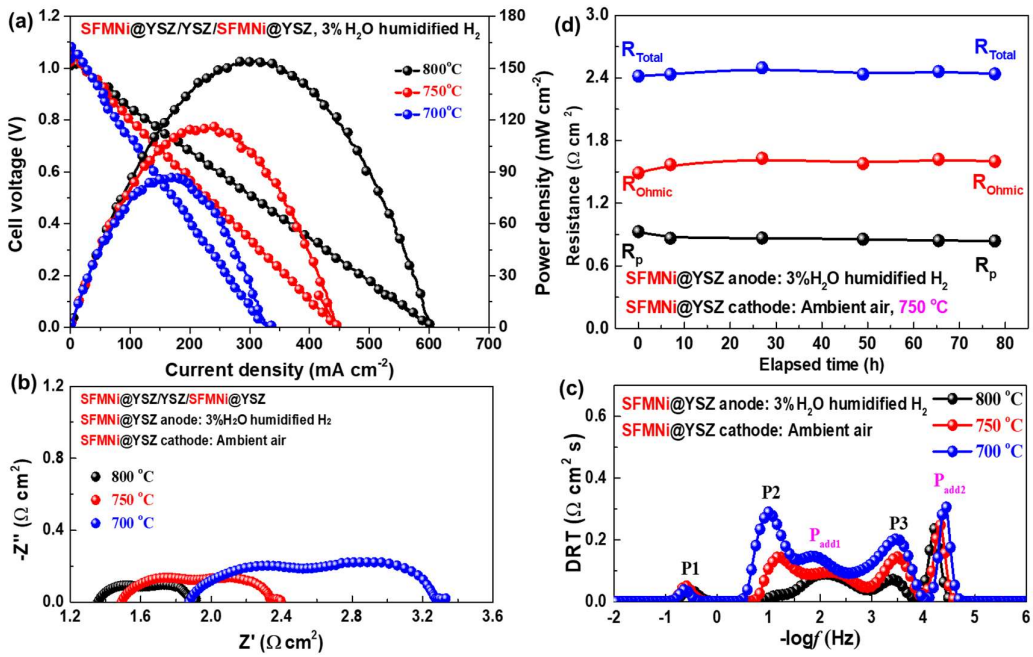

Figure 7 Electrochemical performance of the single cell with a configuration of SFMNi@YSZ/YSZ/SFMNi@YSZ when exposing SFMNi@YSZ anode and SFMNi@YSZ cathode to 3%H_2O humidified H_2 and ambient air, respectively. (a) *i*-V-p curves, (b) the recorded EIS and (c) their corresponding DRT analyst results measured at 700-800 °C with a temperature interval of 50 °C, and (d) the durability of the SFMNi@YSZ symmetrical cell when operated at 750 °C and OCV condition.

Fuel flexibility is a unique advantage of SOFC compared with low-temperature fuel cells. Therefore, we used 3%H_2O wet C_3H_8 (97%C_3H_8-3%H_2O) fuel to verify the feasibility of this cell, and the specific results are shown in Figure 8. The peak power density (P_{max}) of this cell is 100 mW cm^{-2} which is only slightly lower than P_{max} (116 mW cm^{-2}) under 3%H_2O humid H_2, further indicating that the SSOFC can maintain adequate electrochemical performance under propane fuel. At this moment, the current density under a constant discharge voltage of 0.8 V increases slowly from 65 to 72 mA cm^{-2} at the beginning of the test (about 1 hour), which is mainly due to the re-exsolved NiFe nano-catalyst. And then it reaches a plateau and maintains a relatively stable output

performance without significant attenuation when inletting the propane fuel, which is in line with the practical application of SOFCs in the hydrocarbon fuel environment.

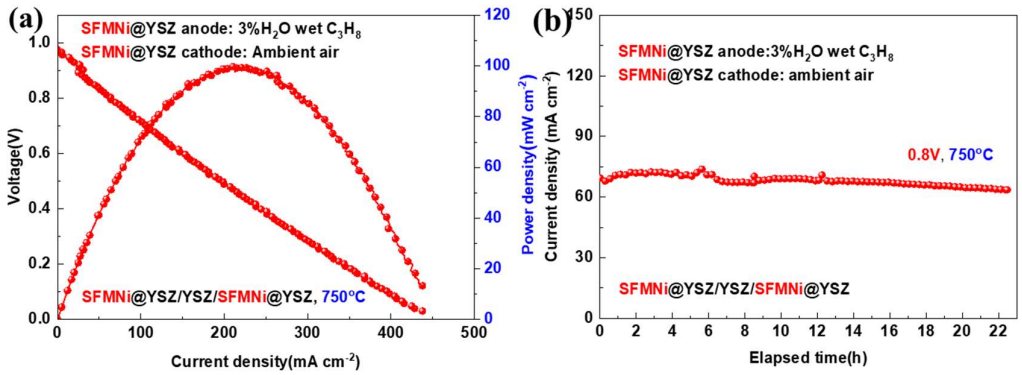

Figure 8 Electrochemical performance of the SFMNi@YSZ symmetrical single cell when exposing SFMNi@YSZ anode and SFMNi@YSZ cathode to 3%H_2O humidified C_3H_8 and ambient air, respectively. (a) *i-V-p* curves, (b) the durability conducted at 750 °C and 0.8 V condition.

4. Conclusions

In this work, a novel SFMNi nanoparticles impregnated hierarchically oriented YSZ electrode with open, straight pores (SFMNi@YSZ electrode) has been successfully developed by combining the novel phase inversion co-tape casting and ion impregnation method, which can be further transformed into *in-situ* exsolved NiFe alloy nanoparticles structured SFMNi@YSZ electrode (NiFe@SFMNi@YSZ electrode) via the *in-situ* exsolution technique. Contact angle and gas permeability results indicate that the excellent microstructure of the YSZ skeleton significantly enhances the gas mass transport process while reducing the difficulty of the infiltration process and improving the dispersion of the impregnated nanoparticles in the skeleton. In addition, the infiltrated SFMNi nano-catalysts, especially the *in-situ* exsolve NiFe alloy catalysts from the infiltrated SFMNi parent material in a reduced atmosphere, could provide more active sites for fuel oxidation, and outputting more excellent electrochemical performance. A low R_p of 0.16 Ω cm^2 is obtained for

this novel electrode when fed with 3%H_2O wet hydrogen at 800°C, and the Rp at 750°C remains stable for nearly 110 hours. Even under the propane fuel atmosphere, its maximum power density can reach 100 mW cm^{-2} at 750°C, which is only 16 mW cm^{-2} lower than that under wet hydrogen. The results indicate that the hierarchically oriented NiFe@SFMNi@YSZ electrode with open, straight pores is a stable and excellent electrode for solid oxide cells to utilize hydrocarbon fuels directly and efficiently.

Declaration of Competing Interest

The authors declare that they have no known competing financial interests or personal relationships that could have appeared to influence the work reported in this paper.

Acknowledgments

This work was supported by National Natural Science Foundation of China (U21A20317, 51602228), the National Key Research and Development Program of China (2022YFA1504701), the Fundamental Research Funds for the Central University (2042022gf0002), the start-up research funds from Wuhan Institute of Technology (K202201) and U.S. National Science Foundation (1832809). The authors also highly thank the Core Facility of Wuhan University for XRD, XPS, and TEM analysis, and Large-scale Instrument & Equipment Sharing Foundation of Wuhan University.

References

[1] A. Bloess, W.-P. Schill, A. Zerrahn, Power-to-heat for renewable energy integration: a review of technologies, modeling approaches, and flexibility potentials, Appl. Energy 212 (2018), 1611-1626. https://doi.org/10.1016/j.apenergy.2017.12.073.

[2] C. Goulart, D. de Souza, Critical analysis of aqueous tape casting, sintering, and characterization of planar yttria-stabilized zirconia electrolytes for SOFC, Int. J. Appl. Ceram. Technol 14(3) (2017), 413-423. https://doi.org/10.1111/ijac.12638.

[3] N. Scarlat, J.-F. Dallemand, F. Fahl, Biogas: developments and perspectives in Europe, Renew. Energ. 129 (2018), 457-472. https://doi.org/10.1016/j.renene.2018.03.006.

[4] Q. Fu, Z. Li, W. Wei, F. Liu, X. Xu, Z. Liu, Performance enhancement of a beam and slot interconnector for anode-supported SOFC stack, Energy Convers. Manage. 241 (2021), 114277. https://doi.org/10.1016/j.enconman.2021.114277.

[5] X. Xu, L. Bi, X.S. Zhao, Highly-conductive proton-conducting electrolyte membranes with a low sintering temperature for solid oxide fuel cells, J. Membr. Sci. 558 (2018), 17-25. https://doi.org/10.1016/j.memsci.2018.04.037.

[6] C. Chatzilias, E. Martino, C.G. Vayenas, G. Kyriakou, A. Katsaounis, A low temperature SOFC as a self-promoted reactor for CO_2 catalytic hydrogenation, Appl. Catal. B 317 (2022), 121778. https://doi.org/10.1016/j.apcatb.2022.121778.

[7] X. Ding, Z. Gao, D. Ding, X. Zhao, H. Hou, S. Zhang, G. Yuan, Cation deficiency enabled fast oxygen reduction reaction for a novel SOFC cathode with promoted CO_2 tolerance, Appl. Catal. B 243 (2019), 546-555. https://doi.org/10.1016/j.apcatb.2018.10.075.

[8] S. Liu, K.T. Chuang, J.-L. Luo, Double-Layered perovskite anode with in situ exsolution of a Co–Fe alloy to cogenerate ethylene and electricity in a proton-conducting ethane fuel cell, ACS Catal 6(2) (2016), 760-768. https://doi.org/10.1021/acscatal.5b02296.

[9] T. Liu, H. Liu, X. Zhang, L. Lei, Y. Zhang, Z. Yuan, F. Chen, Y. Wang, A robust solid oxide electrolyzer for highly efficient electrochemical reforming of methane and steam, J. Mater. Chem. A 7(22) (2019), 13550-13558. https://doi.org/10.1039/C9TA00467J.

[10] N. Yu, T. Liu, X. Chen, M. Miao, M. Ni, Y. Wang, Co-generation of liquid chemicals and electricity over Co-Fe alloy/perovskite anode catalyst in a propane fueled solid oxide fuel cell, Sep. Purif. Technol. 291 (2022), 120890. https://doi.org/10.1016/j.seppur.2022.120890.

[11] N. Shi, Y. Xie, Y. Yang, S. Xue, X. Li, K. Zhu, D. Huan, R. Peng, C. Xia, Y. Lu, Review of anodic reactions in hydrocarbon fueled solid oxide fuel cells and strategies to improve anode performance and stability, Mater Renew Sustain Energy 9(1) (2020), 6. https://doi.org/10.1007/s40243-020-0166-8.

[12] T. Wang, R. Wang, X. Xie, S. Chang, T. Wei, D. Dong, Z. Wang, Robust direct hydrocarbon solid oxide fuel cells with exsolved anode nanocatalysts, ACS Appl. Mater. Interfaces 14(51) (2022), 56735-56742. https://doi.org/10.1021/acsami.2c16284.

[13] C.-H. Kim, J.-Y. Han, H. Lim, K.-Y. Lee, S.-K. Ryi, Hydrogen production by steam methane reforming in membrane reactor equipped with Pd membrane deposited on NiO/YSZ/NiO multilayer-treated porous stainless steel, J. Membr. Sci. 563 (2018), 75-82. https://doi.org/10.1016/j.memsci.2018.05.037.

[14] K.K. Chen, W. Salim, Y. Han, M. Gasda, W.S.W. Ho, Fluoride- and hydroxide-containing CO_2-selective membranes for improving H_2 utilization of solid oxide fuel cells, J. Membr. Sci. 612 (2020), 118484. https://doi.org/10.1016/j.memsci.2020.118484.

[15] X. Wang, K. Wei, S. Yan, Y. Wu, J. Kang, P. Feng, S. Wang, F. Zhou, Y. Ling, Efficient and stable conversion of oxygen-bearing low-concentration coal mine methane by the electrochemical catalysis of SOFC anode: From pollutant to clean energy, Appl. Catal. B 268 (2020), 118413. https://doi.org/10.1016/j.apcatb.2019.118413.

[16] Q. Bkour, F. Che, K.-M. Lee, C. Zhou, N. Akter, J.A. Boscoboinik, K. Zhao, J.T. Gray, S.R. Saunders, M. Grant Norton, J.-S. McEwen, T. Kim, S. Ha, Enhancing the partial oxidation of gasoline with Mo-doped Ni catalysts for SOFC applications: An integrated experimental and DFT study, Appl. Catal. B 266 (2020), 118626. https://doi.org/10.1016/j.apcatb.2020.118626.

[17] H. Mohammed, A. Al-Othman, P. Nancarrow, M. Tawalbeh, M. El Haj Assad, Direct hydrocarbon fuel cells: a promising technology for improving energy efficiency, Energy 172 (2019), 207-219. https://doi.org/10.1016/j.energy.2019.01.105.

[18] H. Su, Y.H. Hu, Progress in low-temperature solid oxide fuel cells with hydrocarbon fuels, Chem. Eng. J. 402 (2020), 126235. https://doi.org/10.1016/j.cej.2020.126235.

[19] W. Zhang, X. Hu, Y. Zhou, Z. Luo, G. Nam, Y. Ding, T. Li, Z. Liu, Y. Ahn, N. Kane, W. Wang, J. Hou, D. Spradling, M. Liu, A solid oxide fuel cell runs on hydrocarbon fuels with exceptional durability and power output, Adv. Energy Mater. 12(47) (2022), 2202928. https://doi.org/10.1002/aenm.202202928.

[20] X.-M. Ge, S.-H. Chan, Q.-L. Liu, Q. Sun, Solid oxide fuel cell anode materials for direct hydrocarbon utilization, Adv. Energy Mater. 2(10) (2012), 1156-1181. https://doi.org/10.1002/aenm.201200342.

[21] B. Meng, H. Zhang, J. Qin, X. Tan, R. Ran, S. Liu, The catalytic effects of $La_{0.3}Sr_{0.7}Fe_{0.7}Cu_{0.2}Mo_{0.1}O_3$ perovskite and its hollow fibre membrane for air separation and methane conversion reactions, Sep. Purif. Technol. 147 (2015), 406-413. https://doi.org/10.1016/j.seppur.2015.01.039.

[22] N. Shi, F. Su, D. Huan, Y. Xie, J. Lin, W. Tan, R. Peng, C. Xia, C. Chen, Y. Lu, Performance and DRT analysis of P-SOFCs fabricated using new phase inversion combined tape casting technology, J. Mater. Chem. A 5(37) (2017), 19664-19671. https://doi.org/10.1039/C7TA04967F.

[23] C. Cui, Y. Wang, Y. Tong, S. Wang, C. Chen, Z. Zhan, Syngas production through CH_4-assisted co-electrolysis of H_2O and CO_2 in $La_{0.8}Sr_{0.2}Cr_{0.5}Fe_{0.5}O_{3-\delta}$-$Zr_{0.84}Y_{0.16}O_{2-\delta}$ electrode-supported solid oxide electrolysis cells, Int. J. Hydrog. Energy 46(39) (2021), 20305-20312. https://doi.org/10.1016/j.ijhydene.2021.03.177.

[24] Z. Zhan, S.A. Barnett, Use of a catalyst layer for propane partial oxidation in solid oxide fuel cells, Solid State Ionics 176(9) (2005), 871-879. https://doi.org/10.1016/j.ssi.2004.12.005.

[25] G. Brus, K. Miyawaki, H. Iwai, M. Saito, H. Yoshida, Tortuosity of an SOFC anode estimated from saturation currents and a mass transport model in comparison with a real micro-structure, Solid State Ionics 265 (2014), 13-21. https://doi.org/10.1016/j.ssi.2014.07.002.

[26] N. Shi, Y. Xie, Y. Yang, D. Huan, Y. Pan, R. Peng, C. Xia, C. Chen, Z. Zhan, Y. Lu, Infiltrated $Ni_{0.08}Co_{0.02}CeO_{2-x}$@$Ni_{0.8}Co_{0.2}$ Catalysts for a finger-like anode in direct methane-fueled solid oxide fuel cells, ACS Appl. Mater. Interfaces 13(4) (2021), 4943-4954. https://doi.org/10.1021/acsami.0c17339.

[27] Y. Liu, Y. Guo, R. Ran, Z. Shao, A novel approach for substantially improving the sinterability of $BaZr_{0.4}Ce_{0.4}Y_{0.2}O_{3-\delta}$ electrolyte for fuel cells by impregnating the green membrane with zinc nitrate as a sintering aid, J. Membr. Sci. 437 (2013), 189-195. https://doi.org/10.1016/j.memsci.2013.03.002.

[28] F. Schulze-Küppers, S. Baumann, W.A. Meulenberg, D. Stöver, H.P. Buchkremer, Manufacturing and performance of advanced supported $Ba_{0.5}Sr_{0.5}Co_{0.8}Fe_{0.2}O_{3-\delta}$ (BSCF) oxygen transport membranes, J. Membr. Sci. 433 (2013), 121-125. https://doi.org/10.1016/j.memsci.2013.01.028.

[29] F. Schulze-Küppers, S. Baumann, W.A. Meulenberg, H.J.M. Bouwmeester, Influence of support

layer resistance on oxygen fluxes through asymmetric membranes based on perovskite-type oxides $SrTi_{1-x}Fe_xO_{3-\delta}$, J. Membr. Sci. 596 (2020), 117704. https://doi.org/10.1016/j.memsci.2019.117704.

[30] C. Zuo, S. Zha, M. Liu, M. Hatano, M. Uchiyama, $Ba(Zr_{0.1}Ce_{0.7}Y_{0.2})O_{3-\delta}$ as an Electrolyte for low-temperature solid-oxide fuel cells, Adv. Mater. 18(24) (2006), 3318-3320. https://doi.org/10.1002/adma.200601366.

[31] C. Xu, W. Sun, R. Ren, X. Yang, M. Ma, J. Qiao, Z. Wang, S. Zhen, K. Sun, A highly active and carbon-tolerant anode decorated with in situ grown cobalt nano-catalyst for intermediate-temperature solid oxide fuel cells, Appl. Catal. B 282 (2021), 119553. https://doi.org/10.1016/j.apcatb.2020.119553.

[32] Y. Yang, T. Li, P. Feng, X. Wang, S. Wang, Y. Ling, Z. Shao, Highly efficient conversion of oxygen-bearing low concentration coal-bed methane into power via solid oxide fuel cell integrated with an activated catalyst-modified anode microchannel, Appl. Energy 328 (2022), 120134. https://doi.org/10.1016/j.apenergy.2022.120134.

[33] F. Yu, J. Xiao, Y. Zhang, W. Cai, Y. Xie, N. Yang, J. Liu, M. Liu, New insights into carbon deposition mechanism of nickel/yttrium-stabilized zirconia cermet from methane by in situ investigation, Appl. Energy 256 (2019), 113910. https://doi.org/10.1016/j.apenergy.2019.113910.

[34] L. Adijanto, A. Sampath, A.S. Yu, M. Cargnello, P. Fornasiero, R.J. Gorte, J.M. Vohs, Synthesis and Stability of $Pd@CeO_2$ Core–Shell Catalyst Films in Solid Oxide Fuel Cell Anodes, ACS Catal 3(8) (2013), 1801-1809. https://doi.org/10.1021/cs4004112.

[35] S. Tao, J.T. Irvine, A redox-stable efficient anode for solid-oxide fuel cells, Nature materials 2(5) (2003), 320-323. https://doi.org/10.1038/nmat871.

[36] P.I. Cowin, C.T. Petit, R. Lan, J.T. Irvine, S. Tao, Recent progress in the development of anode materials for solid oxide fuel cells, Adv. Energy Mater. 1(3) (2011), 314-332. https://doi.org/10.1002/aenm.201100108.

[37] D. Ding, X. Li, S.Y. Lai, K. Gerdes, M. Liu, Enhancing SOFC cathode performance by surface modification through infiltration, Energy Environ. Sci. 7(2) (2014), 552-575. https://doi.org/10.1039/C3EE42926A.

[38] L. Zhang, S. Hu, Z. Cao, B. Pang, J. Wang, P. Zhang, X. Zhu, W. Yang, Repeatable preparation of defect-free electrolyte membranes for proton-conducting fuel cells, J. Membr. Sci. 656 (2022), 120642. https://doi.org/10.1016/j.memsci.2022.120642.

[39] M. Ouyang, P. Boldrin, R.C. Maher, X. Chen, X. Liu, L.F. Cohen, N.P. Brandon, A mechanistic study of the interactions between methane and nickel supported on doped ceria, Appl. Catal. B 248 (2019), 332-340. https://doi.org/10.1016/j.apcatb.2019.02.038.

[40] X. Hu, Y. Xie, Y. Wan, Y. Yang, X. Wu, C. Xia, Antimony-doped strontium cobalt oxide as promising cathode for low-temperature solid oxide fuel cell with excellent carbon dioxide tolerance, Appl. Catal. B 286 (2021), 119901. https://doi.org/10.1016/j.apcatb.2021.119901.

[41] D. Fan, F. Liu, J. Li, T. Wei, Z. Ye, Z. Wang, X. Hu, D. Dong, H. Wang, Z. Shao, A microchannel reactor-integrated ceramic fuel cell with dual-coupling effect for efficient power and syngas co-generation from methane, Appl. Catal. B 297 (2021), 120443. https://doi.org/10.1016/j.apcatb.2021.120443.

[42] N. Yan, J. Pandey, Y. Zeng, B.S. Amirkhiz, B. Hua, N.J. Geels, J.-L. Luo, G. Rothenberg, Developing a thermal- and coking-resistant cobalt–tungsten bimetallic anode catalyst for solid oxide fuel cells, ACS Catal 6(7) (2016), 4630-4634. https://doi.org/10.1021/acscatal.6b01197.

[43] B. Li, S. He, J. Li, X. Yue, J.T.S. Irvine, D. Xie, J. Ni, C. Ni, A Ce/Ru codoped $SrFeO_{3-\delta}$ perovskite for a coke-resistant anode of a symmetrical solid oxide fuel cell, ACS Catal 10(24) (2020), 14398-14409.

https://doi.org/10.1021/acscatal.0c03554.
[44] W. Zhu, C. Xia, J. Fan, R. Peng, G. Meng, Ceria coated Ni as anodes for direct utilization of methane in low-temperature solid oxide fuel cells, J. Power Sources 160(2) (2006), 897-902. https://doi.org/10.1016/j.jpowsour.2006.02.020.
[45] Y. Chen, Y. Zhang, Y. Lin, Z. Yang, D. Su, M. Han, F. Chen, Direct-methane solid oxide fuel cells with hierarchically porous Ni-based anode deposited with nanocatalyst layer, Nano Energy 10 (2014), 1-9. https://doi.org/10.1016/j.nanoen.2014.08.016.
[46] D. Neagu, T.-S. Oh, D.N. Miller, H. Ménard, S.M. Bukhari, S.R. Gamble, R.J. Gorte, J.M. Vohs, J.T.S. Irvine, Nano-socketed nickel particles with enhanced coking resistance grown in situ by redox exsolution, Nat. Commun. 6(1) (2015), 8120. https://doi.org/10.1038/ncomms9120.
[47] C. Zhao, Y. Li, W. Zhang, Y. Zheng, X. Lou, B. Yu, J. Chen, Y. Chen, M. Liu, J. Wang, Heterointerface engineering for enhancing the electrochemical performance of solid oxide cells, Energy Environ. Sci. 13(1) (2020), 53-85. https://doi.org/10.1039/C9EE02230A.
[48] T. Zhu, H.E. Troiani, L.V. Mogni, M. Han, S.A. Barnett, Ni-substituted Sr (Ti, Fe) O_3 SOFC anodes: achieving high performance via metal alloy nanoparticle exsolution, Joule 2(3) (2018), 478-496. https://doi.org/10.1016/j.joule.2018.02.006.
[49] O. Kwon, S. Sengodan, K. Kim, G. Kim, H.Y. Jeong, J. Shin, Y.-W. Ju, J.W. Han, G. Kim, Exsolution trends and co-segregation aspects of self-grown catalyst nanoparticles in perovskites, Nat. Commun. 8(1) (2017), 1-7. https://doi.org/10.1038/ncomms15967.
[50] H.A. Ishfaq, M.Z. Khan, Y.M. Shirke, S. Qamar, A. Hussain, M.T. Mehran, R.-H. Song, M. Saleem, A heuristic approach to boost the performance and Cr poisoning tolerance of solid oxide fuel cell cathode by robust multi-doped ceria coating, Appl. Catal. B 323 (2023), 122178. https://doi.org/10.1016/j.apcatb.2022.122178.
[51] M. Liang, Y. Zhu, Y. Song, D. Guan, Z. Luo, G. Yang, S.P. Jiang, W. Zhou, R. Ran, Z. Shao, A new durable surface nanoparticles‐modified perovskite cathode for protonic ceramic fuel cells from selective cation exsolution under oxidizing atmosphere, Adv. Mater. 34(10) (2022), 2106379. https://doi.org/10.1002/adma.202106379.
[52] M. Qin, Y. Xiao, H. Yang, T. Tan, Z. Wang, X. Fan, C. Yang, Ru/Nb co-doped perovskite anode: Achieving good coking resistance in hydrocarbon fuels via core-shell nanocatalysts exsolution, Appl. Catal. B 299 (2021), 120613. https://doi.org/10.1016/j.apcatb.2021.120613.
[53] K.J. Kim, M.K. Rath, H.H. Kwak, H.J. Kim, J.W. Han, S.-T. Hong, K.T. Lee, A highly active and redox-stable $SrGdNi_{0.2}Mn_{0.8}O_{4\pm\delta}$ anode with in situ exsolution of nanocatalysts, ACS Catal 9(2) (2019), 1172-1182. https://doi.org/10.1021/acscatal.8b03669.
[54] H. Hu, M. Li, H. Min, X. Zhou, J. Li, X. Wang, Y. Lu, X. Ding, Enhancing the catalytic activity and coking tolerance of the perovskite anode for solid oxide fuel cells through in situ exsolution of Co-Fe nanoparticles, ACS Catal 12(1) (2022), 828-836. https://doi.org/10.1021/acscatal.1c04807.
[55] Y. Yang, F. Liu, X. Han, X. Wang, D. Dong, Y. Chen, P. Feng, M. Khan, S. Wang, Y. Ling, Highly efficient and stable fuel-catalyzed dendritic microchannels for dilute ethanol fueled solid oxide fuel cells, Appl. Energy 307 (2022), 118222. https://doi.org/10.1016/j.apenergy.2021.118222.
[56] A.N. Tabish, L. Fan, I. Farhat, M. Irshad, S.Z. Abbas, Computational fluid dynamics modeling of anode-supported solid oxide fuel cells using triple-phase boundary-based kinetics, J. Power Sources 513 (2021), 230564. https://doi.org/10.1016/j.jpowsour.2021.230564.
[57] B. Chen, H. Xu, M. Ni, Modelling of finger-like channelled anode support for SOFCs application, Sci. Bull. 61(17) (2016), 1324-1332. https://doi.org/10.1007/s11434-016-1131-x.

[58] H. Hwang, J. Ahn, H. Lee, J. Oh, J. Kim, J.-P. Ahn, H.-K. Kim, J.-H. Lee, Y. Yoon, J.-H. Hwang, Deep learning-assisted microstructural analysis of Ni/YSZ anode composites for solid oxide fuel cells, Mater. Charact. 172 (2021), 110906. https://doi.org/10.1016/j.matchar.2021.110906.

[59] C. Jin, J. Liu, L. Li, Y. Bai, Electrochemical properties analysis of tubular NiO–YSZ anode-supported SOFCs fabricated by the phase-inversion method, J. Membr. Sci. 341(1) (2009), 233-237. https://doi.org/10.1016/j.memsci.2009.06.012.

[60] Y. Wang, T. Liu, M. Li, C. Xia, B. Zhou, F. Chen, Exsolved Fe–Ni nano-particles from $Sr_2Fe_{1.3}Ni_{0.2}Mo_{0.5}O_6$ perovskite oxide as a cathode for solid oxide steam electrolysis cells, J. Mater. Chem. A 4(37) (2016), 14163-14169. https://doi.org/10.1039/C6TA06078A.

[61] X. Sun, H. Chen, Y. Yin, M.T. Curnan, J.W. Han, Y. Chen, Z. Ma, Progress of exsolved metal nanoparticles on oxides as high performance (electro)catalysts for the conversion of small molecules, Small 17(10) (2021), 2005383. https://doi.org/10.1002/smll.202005383.

[62] N. Dai, J. Feng, Z. Wang, T. Jiang, W. Sun, J. Qiao, K. Sun, Synthesis and characterization of B-site Ni-doped perovskites $Sr_2Fe_{1.5-x}Ni_xMo_{0.5}O_{6-\delta}$ (x = 0, 0.05, 0.1, 0.2, 0.4) as cathodes for SOFCs, J. Mater. Chem. A 1(45) (2013), 14147-14153. https://doi.org/10.1039/C3TA13607H.

[63] Z. Du, H. Zhao, S. Yi, Q. Xia, Y. Gong, Y. Zhang, X. Cheng, Y. Li, L. Gu, K. Świerczek, High-performance anode material $Sr_2FeMo_{0.65}Ni_{0.35}O_{6-\delta}$ with in situ exsolved nanoparticle catalyst, ACS Nano 10(9) (2016), 8660-8669. https://doi.org/10.1021/acsnano.6b03979.

[64] T. Liu, Y. Zhao, X. Zhang, H. Zhang, G. Jiang, W. Zhao, J. Guo, F. Chen, M. Yan, Y. Zhang, Y. Wang, Robust redox-reversible perovskite type steam electrolyser electrode decorated with in situ exsolved metallic nanoparticles, J. Mater. Chem. A 8(2) (2020), 582-591. https://doi.org/10.1039/C9TA06309A.

[65] S. Zhai, H. Xie, B. Chen, M. Ni, A rational design of FeNi alloy nanoparticles and carbonate-decorated perovskite as a highly active and coke-resistant anode for solid oxide fuel cells, Chem. Eng. J. 430 (2022), 132615. https://doi.org/10.1016/j.cej.2021.132615.

[66] Q. Liu, X. Dong, G. Xiao, F. Zhao, F. Chen, A Novel Electrode Material for Symmetrical SOFCs, Adv. Mater. 22(48) (2010), 5478-5482. https://doi.org/10.1002/adma.201001044.

[67] J. Feng, G. Yang, N. Dai, Z. Wang, W. Sun, D. Rooney, J. Qiao, K. Sun, Investigation into the effect of Fe-site substitution on the performance of $Sr_2Fe_{1.5}Mo_{0.5}O_{6-\delta}$ anodes for SOFCs, J. Mater. Chem. A 2(41) (2014), 17628-17634. https://doi.org/10.1039/C4TA03216K.

[68] M.B. Hanif, J.-T. Gao, K. Shaheen, Y.-P. Wang, M. Yasir, S.-L. Zhang, C.-J. Li, C.-X. Li, Performance evaluation of highly active and novel $La_{0.7}Sr_{0.3}Ti_{0.1}Fe_{0.6}Ni_{0.3}O_{3-\delta}$ material both as cathode and anode for intermediate-temperature symmetrical solid oxide fuel cell, J. Power Sources 472 (2020), 228498. https://doi.org/10.1016/j.jpowsour.2020.228498.

[69] Y. Zhou, X. Meng, X. Ye, J. Li, S. Wang, Z. Zhan, Metal-supported solid oxide fuel cells with impregnated $SrFe_{0.75}Mo_{0.25}O_3$ cathodes, J. Power Sources 247 (2014), 556-561. https://doi.org/10.1016/j.jpowsour.2013.08.134.

[70] C. Yang, Z. Yang, C. Jin, G. Xiao, F. Chen, M. Han, Sulfur-tolerant redox-reversible anode material for direct hydrocarbon solid oxide fuel cells, Adv. Mater. 24(11) (2012), 1439-1443. https://doi.org/10.1002/adma.201104852.

[71] B. He, L. Zhao, S. Song, T. Liu, F. Chen, C. Xia, $Sr_2Fe_{1.5}Mo_{0.5}O_{6-\delta}$ - $Sm_{0.2}Ce_{0.8}O_{1.9}$ composite anodes for intermediate-temperature solid oxide fuel cells, J. Electrochem. Soc. 159(5) (2012), B619. https://doi.org/10.1149/2.020206jes.

[72] D.A. Osinkin, S.M. Beresnev, A.V. Khodimchuk, I.V. Korzun, N.I. Lobachevskaya, A.Y. Suntsov, Functional properties and electrochemical performance of Ca-doped $Sr_{2-x}Ca_xFe_{1.5}Mo_{0.5}O_{6-\delta}$ as anode for

solid oxide fuel cells, J. Solid State Electrochem. 23(2) (2019), 627-634. https://doi.org/10.1007/s10008-018-04169-2.

[73] G. Miao, C. Yuan, T. Chen, Y. Zhou, W. Zhan, S. Wang, $Sr_2Fe_{1+x}Mo_{1-x}O_{6-\delta}$ as anode material of cathode–supported solid oxide fuel cells, Int. J. Hydrog. Energy 41(2) (2016), 1104-1111. https://doi.org/10.1016/j.ijhydene.2015.12.045.

[74] X. Meng, Y. Wang, Y. Zhao, T. Zhang, N. Yu, X. Chen, M. Miao, T. Liu, In-situ exsolution of nanoparticles from Ni substituted $Sr_2Fe_{1.5}Mo_{0.5}O_6$ perovskite oxides with different Ni doping contents, Electrochim. Acta 348 (2020), 136351. https://doi.org/10.1016/j.electacta.2020.136351.

[75] T. Zhang, Y. Zhao, X. Zhang, H. Zhang, N. Yu, T. Liu, Y. Wang, Thermal stability of an in situ exsolved metallic nanoparticle structured perovskite type hydrogen electrode for solid oxide cells, ACS Sustain. Chem. Eng. 7(21) (2019), 17834-17844. https://doi.org/10.1021/acssuschemeng.9b04350.

[76] A. Hauch, A. Hagen, J. Hjelm, T. Ramos, Sulfur poisoning of SOFC anodes: effect of overpotential on long-term degradation, J. Electrochem. Soc. 161(6) (2014), F734. https://doi.org/10.1149/2.080406jes.

[77] X. Tong, S. Ovtar, K. Brodersen, P.V. Hendriksen, M. Chen, A 4× 4 cm^2 nanoengineered solid oxide electrolysis cell for efficient and durable hydrogen production, ACS Appl. Mater. Interfaces 11(29) (2019), 25996-26004. https://doi.org/10.1021/acsami.9b07749.

[78] I.T. Bello, Y. Song, N. Yu, Z. Li, S. Zhao, A. Maradesa, T. Liu, Z. Shao, M. Ni, Evaluation of the electrocatalytic performance of a novel nanocomposite cathode material for ceramic fuel cells, J. Power Sources 560 (2023), 232722. https://doi.org/10.1016/j.jpowsour.2023.232722.

[79] Z. Liu, D. Cheng, Y. Zhu, M. Liang, M. Yang, G. Yang, R. Ran, W. Wang, W. Zhou, Z. Shao, Robust bifunctional phosphorus-doped perovskite oxygen electrode for reversible proton ceramic electrochemical cells, Chem. Eng. J. 450 (2022), 137787. https://doi.org/10.1016/j.cej.2022.137787.

[80] N. Yu, G. Jiang, T. Liu, X. Chen, M. Miao, Y. Zhang, Y. Wang, Understanding the A-site non-stoichiometry in perovskites: promotion of exsolution of metallic nanoparticles and the hydrogen oxidation reaction in solid oxide fuel cells, Sustain. Energy Fuels 5(2) (2021), 401-411. https://doi.org/10.1039/D0SE01280G.

[81] Y. Song, J. Liu, Y. Wang, D. Guan, A. Seong, M. Liang, M.J. Robson, X. Xiong, Z. Zhang, G. Kim, Z. Shao, F. Ciucci, Nanocomposites: A New Opportunity for Developing Highly Active and Durable Bifunctional Air Electrodes for Reversible Protonic Ceramic Cells, Adv. Energy Mater. 11(36) (2021), 2101899. https://doi.org/10.1002/aenm.202101899.